Homogenisation of masonry structures subjected to seismic loads through matrix/inclusion micromechanics

Anastasios Drougkas [a,*], Vasilis Sarhosis [a], Antonella D'Alessandro [b], Filippo Ubertini [b]

[a] School of Civil Engineering, University of Leeds, Woodhouse Lane, LS2 9JT Leeds, United Kingdom
[b] Department of Civil and Environmental Engineering, University of Perugia, Via G. Duranti 93, 06125 Perugia, Italy

A B S T R A C T

The mechanical properties of masonry, both in the linear elastic range and after the onset of damage, are dependent on the geometric and mechanical properties of its constituent materials: the units and the mortar. Finite element micromodelling, while capable of providing accurate and comprehensive results, is associated with high computational costs and modelling effort. On the other hand, micromechanical homogenisation of the masonry composite provides an attractive alternative to detailed micromodelling, in which the stress and strain interaction between the material phases can be modelled without excessive computational cost and in which interpretation of the damage state of the phases is more straightforward. However, nonlinear micromechanical homogenisation of masonry elements through varied numerical and analytical approaches remains a subject of intense study.

In this paper, an inclusion-based homogenisation scheme for masonry structures is proposed for plane stress conditions. The scheme is combined with constitutive laws for damage in the constituent materials of the masonry composite and implemented in finite element models. The proposed modelling approach is validated in terms of its capacity to predict the elastic properties against experimental results and a finite element benchmark. Finally, finite element analyses of walls subjected to in-plane shear under varying levels of vertical stress are performed and favourably compared with experimental results in terms of predicted capacity and obtained failure mode. The low computational cost of the proposed model makes it suitable for future application in digital twinning operations.

1. Introduction

Masonry structures are often characterised by vulnerability to damage arising from tectonic [23] or induced seismicity [20], differential soil subsidence and uplift [17], material degradation due to aging [34] or fatigue from continuous operation [4]. This vulnerability arises from the inherent characteristics of masonry materials and elements: high mass, high stiffness and tendency to crack under tensile and shear stresses.

Masonry structures are characterised by the complex stress and strain interaction of their main constituent material phases: the mortar in the joints and the units. The complexity of the interaction arises primarily from two factors: a) the mismatch in the elastic properties of the two material phases, the units typically possessing a higher Young's modulus and lower Poisson's ratio than the mortar, and b) the geometric bond pattern, which produces staggered arrangements of head joints

even in simple single-wythe structures. Due to these facts, masonry structures exhibit strong orthotropy in strength and elasticity, even when their constituent materials are isotropic [28,27,32]. This reflects the behaviour of other composite materials comprised of inclusions embedded in a matrix.

Due to the differences in the mechanical properties and durability of the constituent materials of masonry, which leads to different rates of degradation and damage in each material phase, early detection of damage in masonry structures requires structural monitoring technologies capable of providing damage sensing at the material level of the mortar or brick [21]. Consequently, numerical analyses accompanying structural health monitoring as the computational component in a digital twinning operation should be able to provide material-level stresses, strains and quantified damage data.

Numerical simulation of masonry structures designed to explicitly take into consideration the properties, geometric arrangement and

---

interaction of the material phases can be performed through the adoption of detailed micromodelling techniques, where the units, mortar and the unit-mortar interface are all explicitly modelled [14,15,24,36]. However, this approach is burdened by excessive computational cost for modelling large structures, in addition to requiring substantial effort for the interpretation of the acquired numerical results.

Computational costs for determining the orthotropic elastic properties of masonry or for carrying out nonlinear analyses may be reduced through the adoption of micromechanical analysis techniques, both for regularly [2,10,35,39] and for irregularly [8,9] bonded masonry. These techniques may be based on a closed form calculation of the stresses and strains in the components or through a statistical averaging process. It has been shown that very satisfactory results compared to detailed micromodelling, as well as efficient scale coupling, can be achieved through such methods with only a small number of assumptions or simplifications [1,33].

The observation that masonry can be treated as a composite material, consisting of unit inclusions embedded in a mortar matrix [19,29], has led to the use of homogenisation schemes based on matrix/inclusion modelling for the analysis of masonry structures [6,7,16] as an alternative to detailed micromodelling. However, these efforts relied on the assumption that the units, which are typically cuboidal in shape (or rectangular in plane strain), can be treated as oblate spheroids (or ellipsoids in plane strain). Additionally, in the cases where nonlinear analysis was attempted, it was limited to material-level predictions of the compressive strength rather than the implementation of the homogenisation scheme for the analysis of full masonry structural elements.

In this paper a modelling approach for masonry structures based on inclusion micromechanics is presented in combination with nonlinear material constitutive laws. The first aim of the study is to verify the validity of the homogenisation scheme for rectangular inclusions depending on the masonry geometric bond pattern. The second aim is to implement the scheme and constitutive laws in a finite element context for the low-cost analysis of large masonry structures and to validate the approach's suitability for reproducing damage typically arising from seismic excitation of masonry shear walls.

The paper begins with the description of the homogenisation scheme for deriving the stiffness tensor in plane stress of the masonry composite from the geometric and material properties of the constituent materials, taking into account the rectangular shape of the units. Next, the nonlinear constitutive laws for describing the stress–strain behaviour of the materials in tension and compression are presented in a damage mechanics context. The description of the implementation of the scheme and constitutive laws for plane stress finite element analysis is subsequently presented. Finally, the proposed model is validated firstly in its capacity to predict the elastic properties of masonry through a comparison with experimental case studies and a finite element benchmark and secondly in its capacity to predict the behaviour of masonry walls subjected to in-plane shear under varying levels of vertical prestress in terms of predicted peak force and failure mode. Additional commentary is provided regarding the interpretation of the quantitative damage predictions of the model.

2. Micromechanical homogenisation scheme

At the macro scale, masonry is treated as a composite material consisting of two material phases interacting in the micro scale: the mortar in the joints and the units. Regularly bonded single wythe masonry structures are treated in this paper. An illustration of the masonry composite material and its constituent material phases is shown in Fig. 1.

In the inclusion approach to micromechanics, a single isotropic inclusion is embedded in an isotropic matrix with infinite dimensions. Generally, the matrix and the inclusion have different elastic properties, the latter acting as a reinforcing agent for the former. When the matrix undergoes a mean deformation, expressed in the strain vector ε, the inclusion is, in turn, deformed as well. Due to the two phases having different elastic properties, the average strain in the inclusion is different to the average strain in the matrix that constrains it. Upon removal of this constraint, the inclusion assumes a strain state called eigenstrain ε^*. The average matrix strain and the eigenstrain are related through the equation:

$$\varepsilon_{ij} = S_{ijkl}\varepsilon^*_{kl} \tag{1}$$

where S_{ijkl} are the components of the fourth order Eshelby's tensor S [19]. Closed form expressions for a rectangular inclusion with height h along the y-axis and length l along the x-axis in plane strain in the xy plane have been recently elaborated. These expressions are material independent with regard to the material properties of the inclusion and are a function of its geometric aspect. Eshelby's tensor S can be decomposed into an isotropic part S_I and a deviatoric part S_D [40]. Expressed in tensor form, these parts are equal to [41]:

$$S = S_I + S_D$$

$$S_I = \frac{1}{8(1+\nu_m)}\begin{bmatrix} 5-4\nu_m & 4\nu_m-1 & 0 \\ 4\nu_m-1 & 5-4\nu_m & 0 \\ 0 & 0 & 3-4\nu_m \end{bmatrix}$$

$$S_D = \frac{1}{1-\nu_m}\begin{bmatrix} (1-\nu_m)p_2+p_4 & \nu_m p_2-p_4 & \frac{1-2\nu_m}{2}q_2+q_4 \\ -\nu_m p_2-p_4 & -(1-\nu_m)p_2+p_4 & \frac{1-2\nu_m}{2}q_2-q_4 \\ \frac{1}{2}q_2+q_4 & \frac{1}{2}q_2-q_4 & -p_4 \end{bmatrix} \tag{2}$$

where ν_m is the Poisson's ratio of the matrix and [18]:

$$p_2 = \frac{2}{\pi}\left(\arctan(\eta)-\frac{\pi}{4}\right) - \frac{1}{2\pi\eta}\ln(1+\eta^2) + \frac{1}{2\pi}\ln\left(\frac{1+\eta^2}{\eta^2}\right)$$

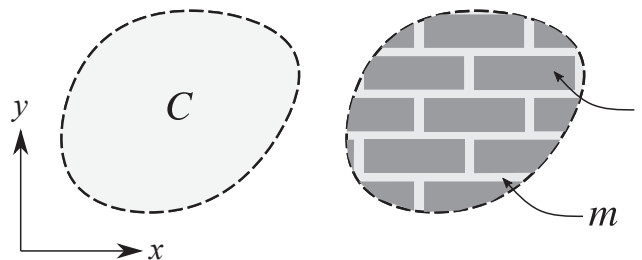$$p_4 = -\frac{1}{8} + \frac{1}{4\pi\eta}\ln(1+\eta^2) + \frac{\eta}{2\pi}\ln\left(\frac{1+\eta^2}{\eta^2}\right)$$

Fig. 1. Masonry composite material (C) and its constituent materials, mortar matrix (m) and unit inclusions (i).

$$q_2 = q_4 = 0 \tag{3}$$

where $\eta = h/l$. For calculating S for plane stress inclusions, ν_m should be replaced with $\nu_m/(1+\nu_m)$ in the above equations.

When multiple inclusions with identical orientation, geometry and elastic properties are evenly distributed in a matrix, these can be treated as a group. The dilute approximation of inclusions states that the dilute estimate T_i of the inclusions i in the matrix m is equal to:

$$T_i = \left(I + S_i(C_m)^{-1}(C_i - C_m)\right)^{-1} \tag{4}$$

where I is the 3×3 identity tensor and C_m and C_i are the plane stress stiffness tensors of the matrix and the inclusion respectively, functions of the Young's moduli and Poisson's ratios of the individual phases. Generally, the isotropic plane stress stiffness tensor C of a material with Young's modulus E and Poisson's ratio ν reads:

$$C = \frac{E}{(1-\nu)^2} \begin{bmatrix} 1 & \nu & 0 \\ \nu & 1 & 0 \\ 0 & 0 & 1-\nu \end{bmatrix} \tag{5}$$

The matrix strain concentration factor A_C is a function of the dilute estimate of the inclusions in the matrix and is equal to:

$$A_C = (\omega_m I + \omega_i T_i)^{-1} \tag{6}$$

where ω_i is the volume ratio of the inclusions and ω_m the volume ratio of the matrix with respect to the total volume of the composite, with $\omega_i + \omega_m = 1$. The strain concentration tensor A_i of the inclusions is equal to:

$$A_i = T_i A_C \tag{7}$$

Finally, the effective stiffness tensor C_C of the composite material can be calculated in closed form according to the equation [26]:

$$C_C = C_m + \omega_i(C_i - C_m)A_i \tag{8}$$

While the stiffness matrices of the matrix and the inclusions may be isotropic, the orthotropy of the masonry composite arises from the difference between the length l_u and height h_u of the units.

In addition to allowing the calculation of the stiffness tensor of the composite material, the above scheme makes it possible to calculate the stress and strain interaction between the inclusions and the matrix. The strain vector in the matrix ε_m is equal to [29]:

$$\varepsilon_m = A_C \varepsilon_C \tag{9}$$

where ε_C is the macroscopic strain vector in the composite. The stress vector σ_m in the matrix is equal to:

$$\sigma_m = C_m \varepsilon_m \tag{10}$$

The strain vector ε_i in the inclusions is equal to [5]:

$$\varepsilon_i = A_i \varepsilon_c \tag{11}$$

and the stress vector in the inclusions σ_i is equal to:

$$\sigma_i = C_i A_i (C_C)^{-1} \sigma_C \tag{12}$$

where σ_C is the macroscopic stress vector in the composite material, equal to:

$$\sigma_C = C_C \varepsilon_C \tag{13}$$

The described homogenisation scheme is applied to masonry walls in plane stress conditions, subjected to in plane loading. The mortar in the joints serves as the matrix and the units serve as the inclusions. Regularly bonded single wythe masonry means that all units are of equal nominal size and oriented with their length along the longitudinal axis of the wall. This precludes any complex calculations regarding orientation of the inclusions with respect to the global axes of the composite. Therefore, the entire scheme can be expressed in convenient closed form.

3. Constitutive modelling

Both the mortar (based on lime, cement or a combination of the two) and the units (typically brick, concrete or stone) in masonry are quasi brittle materials. These materials can fail in compression and tension. Similarly, the unit-mortar interface can fail in tension or shear. A damage mechanics approach is adopted in this paper for calculating and expressing the loss of stiffness in the material phases through the use of integrity variables [38]. Integrity variables are scalars ranging from 1 in the case of an undamaged material and tending to 0 in the case of a fully softened material. These integrity variables are equal to the ratio between the actual damaged stress in the material phase and the effective stress, which is the stress that would arise in the material phase for a given strain if the material were linear elastic, i.e., the effective stress is proportional to the strain. These integrity variables are multiplied with the stiffness tensors of each material phase for calculating the reduced stiffness due to damage. The adoption of integrity variables offers a simple method for damage quantification, namely the constitutive relation between an imposed strain and a percentile loss of stiffness in a material.

Compressive failure in each material phase is modelled through a simple bilinear hardening curve up to peak stress followed by an exponential softening curve based on compressive fracture energy. The integrity variable in compression I_c as a function of the strain ε is equal to:

$$I_c(\varepsilon) = \begin{cases} 1 & \varepsilon_c^l \leq \varepsilon \leq 0 \\ \dfrac{f_c}{\sigma_e}\left(\dfrac{3\varepsilon_c^l - \varepsilon_c^p}{3\varepsilon_c^l - 3\varepsilon_c^p} - \dfrac{2\varepsilon}{3\varepsilon_c^l - 3\varepsilon_c^p}\right) & \varepsilon_c^p \leq \varepsilon \leq \varepsilon_c^l \\ \dfrac{f_c}{\sigma_e}\exp\left(-\dfrac{\varepsilon - \varepsilon_c^p}{\varepsilon_c^u}\right) & \varepsilon \leq \varepsilon_c^p \end{cases} \tag{14}$$

where f_c is the compressive strength of the component (negative value), σ_e is the effective stress and ε_c^l, ε_c^p and ε_c^u being the limit of proportionality, peak strain and ultimate strain in compression respectively, equal to:

$$\varepsilon_c^l = \frac{f_c}{3E}$$

$$\varepsilon_c^p = 5\varepsilon_c^l$$

$$\varepsilon_c^u = \frac{G_c}{f_c h} \tag{15}$$

where E is the Young's modulus, G_c is the compressive fracture energy of the material and h is the bandwidth, namely the length at which the constitutive law is being evaluated.

Tensile damage in each material phase is modelled through linear behaviour up to peak stress followed by an exponential softening curve based on tensile fracture energy. The integrity variable for tension I_t is equal to:

$$I_t(\varepsilon) = \begin{cases} 1 & 0 \leq \varepsilon \leq \varepsilon_t^p \\ \dfrac{f_t}{\sigma_e}\exp\left(-\dfrac{\varepsilon - \varepsilon_t^p}{\varepsilon_t^u}\right) & \varepsilon_t^p \leq \varepsilon \end{cases} \tag{16}$$

where f_t is the tensile strength and ε_t^p and ε_t^u being the peak strain and ultimate strain in tension respectively. These are equal to:

$$\varepsilon_t^p = \frac{f_t}{E_c}$$

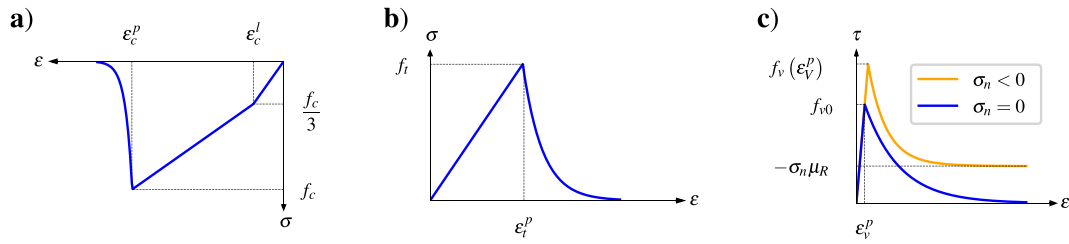$$\varepsilon_t^u = \frac{G_t}{f_t h} \tag{17}$$

Fig. 2. Stress–strain constitutive laws for damage in components: a) compression, b) tension and c) shear.
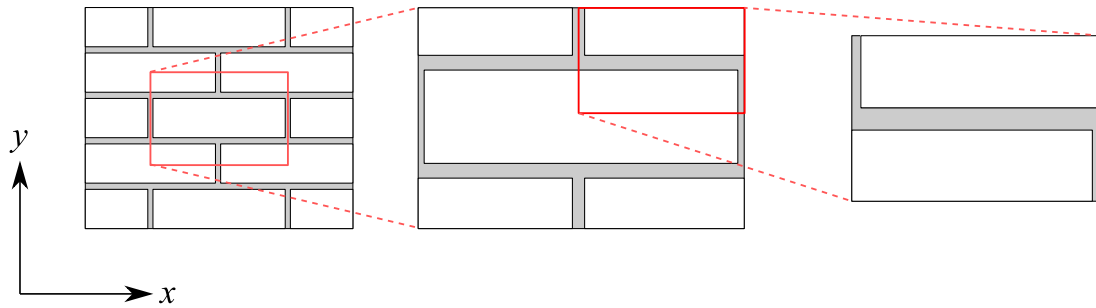

Fig. 3. Derivation of the periodic unit cell for running bond masonry. Extraction of the repeating pattern and reduction due to symmetry of the cell.

where G_t is the tensile fracture energy.

For the shear strength f_v, linear behaviour is assumed up to peak stress, followed by an exponential softening curve. As such, the shear strength as a function of the strain is:

$$f_v(\varepsilon) = \begin{cases} f_{v0} & 0 \leq |\varepsilon| \leq \varepsilon_v^p \\ f_{v0}\exp\left(-\dfrac{|\varepsilon| - \varepsilon_v^p}{\varepsilon_v^u}\right) & \varepsilon_v^p \leq |\varepsilon| \end{cases} \tag{18}$$

where f_{v0} is the initial shear strength of the component (positive) and ε_v^p and ε_v^u being the peak strain and ultimate strain for the shear strength respectively. These are equal to:

$$\varepsilon_v^p = \frac{1+\nu}{E} f_{v0}$$

$$\varepsilon_v^u = \frac{G_v}{f_{v0} h} \tag{19}$$

where G_v is the shear fracture energy. For the friction coefficient μ the constitutive relation reads:

$$\mu(\varepsilon) = \begin{cases} \mu_0 & 0 \leq |\varepsilon| \leq \varepsilon_v^p \\ \mu_0 + \dfrac{(\mu_R - \mu_0)(f_{v0} - f_v(\varepsilon))}{f_{v0}} & \varepsilon_v^p \leq |\varepsilon| \end{cases} \tag{20}$$

where μ_0 and μ_R are the initial and residual values of the friction coefficient respectively. Finally, the integrity variable in shear I_v can be expressed as:

$$I_v(\varepsilon) = \begin{cases} 1 & 0 \leq |\varepsilon| \leq \varepsilon_V^p \\ \dfrac{|\sigma_n|\mu(\varepsilon) + f_{v0}\exp\left(-\dfrac{|\varepsilon| - \varepsilon_V^p}{\varepsilon_v^u}\right)}{|\sigma_e|} & \varepsilon_V^p \leq |\varepsilon| \end{cases} \tag{21}$$

where σ_n is the compressive stress acting normal to the shearing surface (negative for compression, disregarded for tension) and ε_V^p is the peak strain in shear, calculated as:

$$\varepsilon_V^p = \frac{1+\nu}{E}(f_{v0} + |\sigma_n|\mu_0) \tag{22}$$

The constitutive equations for compressive, tensile and shear damage are presented in stress–strain terms in Fig. 2.

4. Finite element implementation

The above presented homogenisation scheme and accompanying constitutive stress–strain laws have been implemented in plane stress in the FEniCS finite element platform [3] for the analysis of structures. The implementation of the model is performed at the Gauss points of the structural mesh. Masonry is treated as a composite material wherein the mortar in the joints acts as the matrix and the units act as the inclusions.

It is assumed that the masonry is regularly bonded with a repeating geometric pattern. Therefore, it is possible to extract a periodic unit cell, representative of the layout of the material phases in the composite. For the case of running bond masonry, this periodic unit cell, and its reduction due to geometric symmetry is illustrated in Fig. 3. Under plane stress conditions, the geometry is not altered along the thickness of the
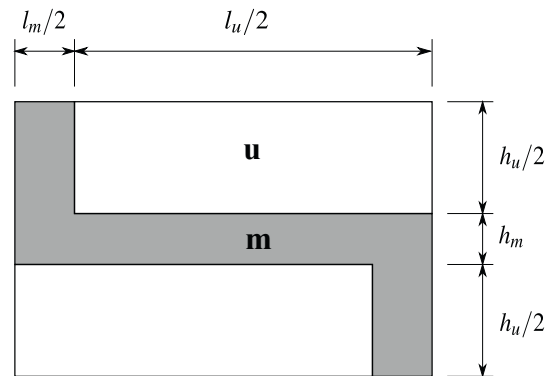

Fig. 4. Dimensions of periodic unit cells and geometric arrangement of material phases: *m* for mortar and *u* for units.

cell perpendicularly to the *xy* plane.

Following the extraction of the periodic unit cell, it is possible to calculate the volume ratios of the mortar matrix and the unit inclusions. As illustrated in Fig. 4, the volume ratio ω_i of the units and ω_m of the mortar in the running bond masonry composite are equal to:

$$\omega_i = \frac{2 \frac{l_u}{2} \frac{h_u}{2}}{\left(\frac{l_u}{2} + \frac{l_m}{2}\right)(h_u + h_m)}$$

$$\omega_m = 1 - \omega_i \tag{23}$$

where l_u is the length of the unit, l_m is the thickness of the head joint, h_u is the height of the unit and h_m is the thickness of the bed joint. For stack bond masonry, the volume ratios can be obtained by assuming $l_m = 0$.

In keeping with the manner in which failure in the masonry components develops, and taking into consideration the regularity of the masonry bond, the constitutive equations for damage are evaluated in the following manner:

1) Mortar is checked in compression in the vertical *y* and horizontal *x* directions, simulating crushing of the bed joints and head joints respectively.
2) Mortar is checked in tension in the vertical *y* and horizontal *x* directions, simulating the opening of the bed joints and head joints

respectively. The mortar is assigned the tensile strength of the unit-mortar interface.
3) Units are checked in compression in the vertical *y* direction, simulating the crushing of the units under vertical load.
4) Units are checked in tension in the horizontal *x* direction, simulating the cracking of the units due to unit-bed joint interaction under compression.
5) The unit-mortar bed joint interface is checked in shear according to the shear strain in the matrix

Through the above evaluations of damage, the mechanical orthotropy of the masonry composite, arising from the homogenisation scheme due to the different dimensions of the units in the *x* and *y* directions, is further reinforced in the nonlinear range. The bandwidths *h* used in eq. (15), (17) and (19) are a function of the dimensions of the material component in the direction where damage is being evaluated [43]. In this context, the bandwidth *h* is equal to:

$$h = \frac{d}{D} l \tag{24}$$

where *d* is the dimension of the component in the direction being evaluated, *D* is the dimension of the periodic unit cell in the direction being evaluated and *l* is the characteristic finite element length where the evaluation is being performed, namely the square root of its surface

Table 1
Model validation: comparison of Young's modulus as experimentally derived (E_{yy}^{exp}) and predicted by the proposed model (E_{yy}^{mod}) and by finite element analysis (E_{yy}^{FE}).

| Parameter	Symbol	Units	Case study									
Reference	–	–	[31]	[22]						[37]	[15]	[12]
Young's modulus of units	E_u	(N/mm²)	6740	3372	3372	3372	976	976	976	4000	4080	2570
Poisson's ratio of units	ν_u	(–)	0.167	0.150	0.150	0.150	0.150	0.150	0.150	0.130	0.150	0.150
Length of units	l_u	(mm)	110	230	230	230	230	230	230	206	72.5	188
Height of units	h_u	(mm)	35	75	75	75	75	75	75	50	12.5	42
Young's modulus of mortar	E_m	(N/mm²)	970	5450	7083	8568	238	1500	8568	1650	3500	920
Poisson's ratio of mortar	ν_m	(–)	0.200	0.200	0.200	0.200	0.200	0.200	0.200	0.200	0.200	0.200
Thickness of head joint	l_m	(mm)	5.0	12.0	12.0	12.0	12.0	12.0	12.0	12.5	2.5	12
Thickness of bed joint	h_m	(mm)	5.0	12.0	12.0	12.0	12.0	12.0	12.0	10.0	2.5	12
Young's modulus of masonry - experiment	E_{yy}^{exp}	(N/mm²)	3700	5232	4824	5024	580	735	400	3200	4370	1615
Young's modulus of masonry – proposed model	E_{yy}^{mod}	(N/mm²)	3655	3645	3785	3888	652	1047	1402	3046	4017	1775
Young's modulus of masonry – FE analysis	E_{yy}^{FE}	(N/mm²)	3936	3660	3702	3782	717	1033	1254	3114	3917	1856
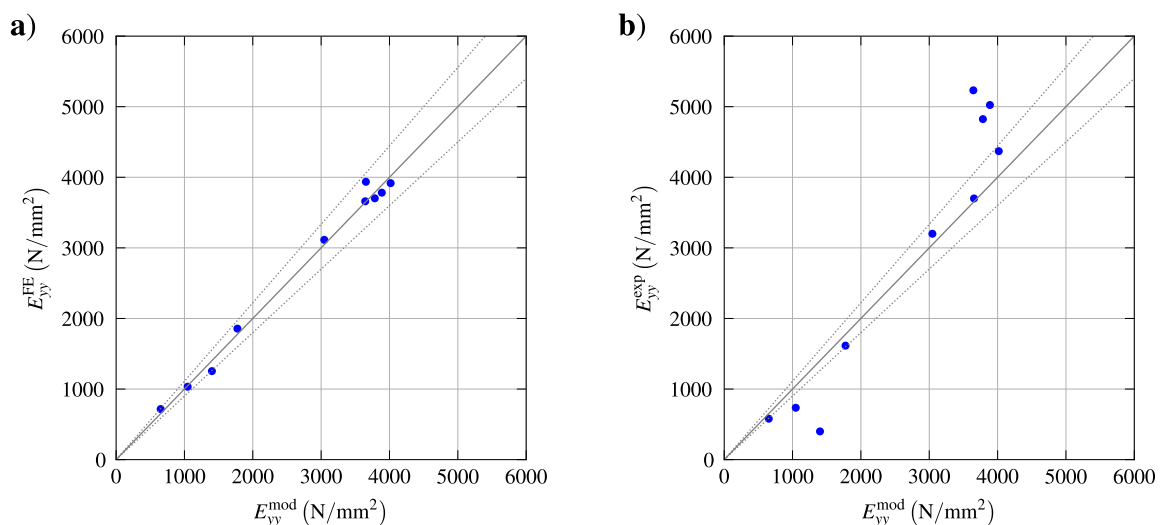
Fig. 5. Linear elastic analysis results for running bond case studies. Comparison of proposed model predictions with a) finite element analyses and b) experimental results. Solid line indicates equality and dotted lines indicate 10% deviation.

Table 2
Geometric and mechanical parameter values used in parametric investigation.

Component	Parameter	Symbol	Value	Units
Units	Young's modulus	E_u	20,000	N/mm²
	Poisson's ratio	ν_u	0.15	N/mm²
	Length	l_u	210	mm
	Height	h_u	52	mm
Mortar	Young's modulus	E_m	20 – 20,000	N/mm²
	Poisson's ratio	ν_m	0.15	N/mm²
	Head joint thickness	l_m	0.1–30	mm
	Bed joint thickness	h_m	0.1–30	mm

area. For example, when the bed joint is being evaluated against vertical compression, $d = h_m$ and $D = h_u + h_m$. In addition to handling orthotropy arising from the masonry bond, this adjustment of the bandwidth is adopted for dealing with scale separation violation arising from the relatively large dimensions of the unit inclusions compared to the thickness of the mortar joint matrix into which they are embedded. Scale separation in masonry multi-scale modelling remains an open problem due to the practical difficulties in reliably determining scale separation limits in periodic masonry through experimental means.

In nonlinear analysis, the damaged stiffness tensors of the units and the mortar are calculated by multiplying the elastic stiffness tensor of each phase calculated from Eq. (5) with the integrity variables calculated for each phase from Eq. (14), (16) and (21) (both units and mortar are evaluated in compression and tension, while mortar is additionally evaluated in shear). This isotropic damage approach means that reduction of the integrity variable in one direction in a given material phase results in the equal reduction of the stiffness of the phase in all directions. Further, the phase-wise calculation of stiffness loss means that damage in the masonry composite cannot be directly expressed in a single scalar value. This is accomplished for each phase through multiplication of its stiffness tensor with all its integrity variable scalars. Finally, damage is irreversible, meaning that reduction of the strain in a component does not lead to a potential increase in the integrity.

5. Model validation

5.1. Linear elastic analysis

The accuracy of the homogenisation scheme in predicting the elastic properties of masonry is evaluated against a series of experimental tests from the literature involving the determination of the Young's modulus
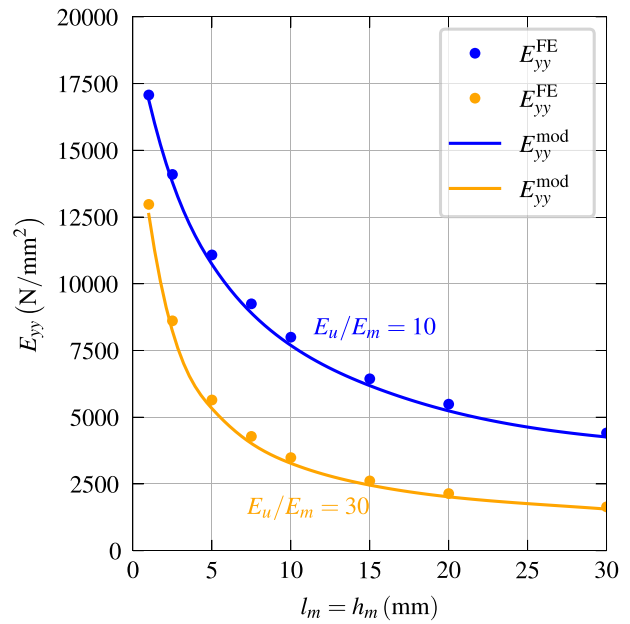

Fig. 7. Results of scale separation investigation.

of masonry in the vertical y direction (E_{yy}). In addition, the same case studies are analysed using finite element mesomodels, namely detailed micromodels without the explicit modelling of the unit-mortar interface, for comparing the results of the proposed model with results from an established analysis method.

These case studies considered [12,15,22,31,37] involve concentric uniform compression tests conducted on single-wythe running bond masonry wallettes in the direction normal to the bed joints. In all cases the wallettes were constructed using solid brick units and lime/cement mortar, with soil introduced in one of the mortars used in one case study [22].

The results of the linear elastic analysis are summarised in Table 1. It is shown that the proposed model predicts the Young's modulus of masonry with substantial accuracy for most cases. Large deviations from the experimental results occur in a few cases, where peculiarly the Young's modulus of masonry was lower than that of either of the constituent materials. Regardless, of special note is the closeness between the results of the proposed model and those of the finite element analysis for all cases. Therefore, it is demonstrated that the proposed model can serve in the task of predicting the Young's modulus of masonry on an
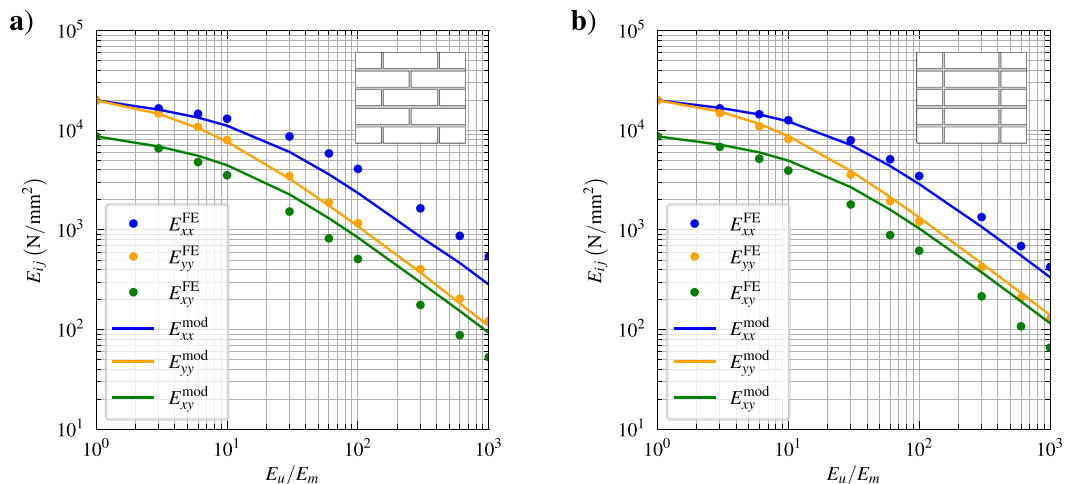

Fig. 6. Results of linear elastic parametric investigation. Comparison of proposed model predictions of elastic moduli against a finite element benchmark: a) running bond and b) stack bond.

Table 3
Geometric and material properties of constituent materials.

Component	Parameter	Symbol	Value	Units
Units	Length	l_u	72.5	mm
	Height	h_u	12.5	mm
	Width	t_u	35.0	mm
	Young's modulus	E_u	4080	N/mm²
	Poisson's ratio	ν_u	0.15	–
	Compressive strength	f_{cu}	−45.57	N/mm²
	Tensile strength	f_{tu}	3.59	N/mm²
	Compressive fracture energy	G_{cu}	45.57	N/mm
	Tensile fracture energy	G_{tu}	0.120	N/mm
Mortar	Head joint thickness	l_m	2.5	mm
	Bed joint thickness	h_m	2.5	mm
	Young's modulus	E_m	3500	N/mm²
	Poisson's ratio	ν_m	0.20	–
	Compressive strength	f_{cm}	−7.44	N/mm²
	Tensile strength	f_{tm}	1.05	N/mm²
	Compressive fracture energy	G_{cm}	7.44	N/mm
	Tensile fracture energy	G_{tm}	0.111	N/mm
Unit-mortar interface	Tensile strength	f_{ti}	0.18	N/mm²
	Tensile fracture energy	G_{ti}	0.013	N/mm
	Initial shear strength	f_{v0}	0.250	N/mm²
	Initial friction coefficient	μ_0	0.815	–
	Residual friction coefficient	μ_R	0.770	–
	Shear fracture energy	G_v	0.300	N/mm

equal footing with finite element analysis, with the added benefits of reduced modelling effort and computational cost. The results of the linear elastic analyses are further illustrated in Fig. 5. The coincidence of the model predictions with the finite element analysis results can be clearly seen.

The accuracy of the model in predicting the elastic moduli of masonry is assessed through a parametric investigation against a finite element benchmark in order to enrich the validation with elastic parameters often not characterised in experimental testing, namely the horizontal Young's modulus of masonry E_{xx} and the shear modulus E_{xy}. The parametric investigation is performed through varying the Young's modulus of the mortar E_m as a ratio of the Young's modulus of the units E_u. The values used in the parametric investigation are presented in Table 2. In the finite element analyses two different geometric patterns were investigated: a running bond pattern, where the units overlap in a staggered arrangement, and a stack bond pattern, in which the units do not overlap but allow the formation of both continuous bed and head joints. The head and bed joint thickness used in this investigation was 10 mm.

The results are illustrated in Fig. 6. For the running bond case, while the vertical Young's modulus of masonry E_{yy} is predicted with excellent accuracy, the horizontal Young's modulus E_{xx} is underestimated by the model as the E_u/E_m ratio increases. This is due to the inability of the model to precisely account for the shear stresses developed in the bed joint under horizontal stressing of the masonry, which contributes to the increase of the horizontal stiffness of the composite material in the presence of unit interlocking [42]. The influence of interlocking becomes more pronounced as the units become relatively stiffer compared to the mortar. A similar overestimation is obtained for the in-plane shear modulus E_{xy}. This overestimation is due to the presence of a continuous bed joint, essentially free to deform in shear, which cannot be directly accounted for by the homogenisation scheme. Nevertheless, these discrepancies only become significant for a Young's modulus of mortar less than 10% with respect to that of the units, which substantially narrows down the cases for which these discrepancies can arise. Conversely, in the stack bond case the prediction of E_{xx} is much more accurate throughout the investigated range. This is due to the shear deformation of the bed joint not playing a significant part in the response of stack bond masonry under horizontal macroscopic stress.

A second sensitivity study was conducted for investigating potential scale separation issues stemming from the mortar matrix surrounding the unit inclusions having dimensions of the same order of magnitude. This investigation was conducted based on the properties listed in Table 2 and varying the head and bed joint thickness and evaluating changes in the vertical Young's modulus E_{yy}. The results of the proposed homogenisation scheme and their comparison with a finite element benchmark for two different ratios of E_u/E_m are illustrated in Fig. 7. The accuracy of the scheme is not affected even for very small matrix volume ratios which do not conform with scale separation conditions.

5.2. Nonlinear analysis of masonry shear walls

The finite element implementation of the homogenisation scheme and constitutive laws are validated against two series of experiments on masonry walls subjected to in plane shear under varying levels of vertical prestress [15]. The experiments were conducted on scaled down single wythe masonry walls constructed in a running bond pattern. The two series of experiments involved solid and perforated walls featuring a single window opening, eccentrically placed with regard to the centre of the wall. The geometric and material properties for the units, mortar and the unit-mortar interface as determined in the experimental campaign and used in the analyses are presented in Table 3. The units were solid clay bricks scaled down to one quarter scale and were subjected to
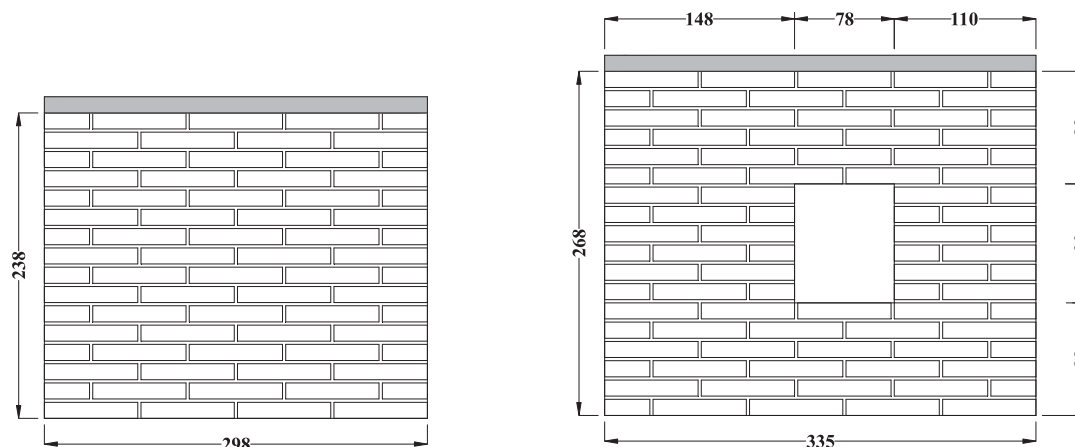
Fig. 8. Geometry of tested masonry solid and perforated walls. Dimensions in **mm**.

Table 4
Comparison of experimental and numerical results for masonry shear walls.

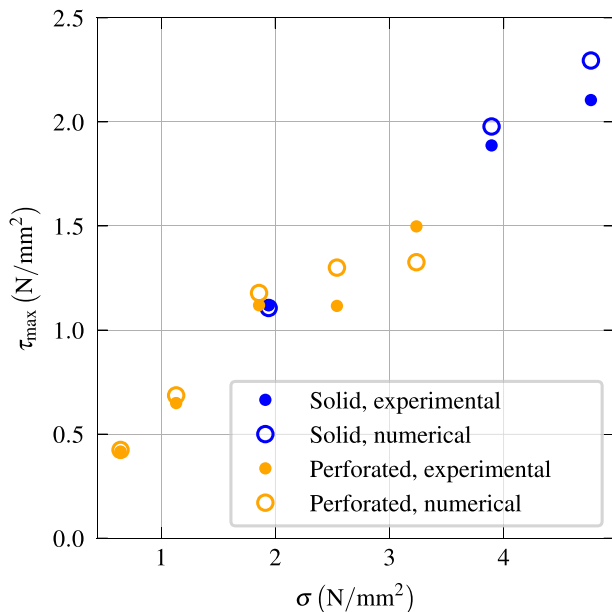| Walls	Specimen	Vertical stress σ (N/mm^2)	Experimental peak shear stress τ_{max}^{exp} (N/mm^2)	Numerical peak shear stress τ_{max}^{num} (N/mm^2)
Solid	2N20	1.942	1.119	1.106
	3N40	3.894	1.887	1.978
	4N50	4.764	2.105	2.295
Perforated	1V7	0.645	0.416	0.424
	2V13	1.132	0.649	0.686
	3V21	1.858	1.119	1.178
	4V30	2.540	1.116	1.209
	5V38	3.236	1.498	1.326

Fig. 9. Interaction diagrams for masonry walls between vertical prestress σ and peak stress τ_{max} as obtained in the experiments and predicted by the proposed model.

compressive and flexural testing. The mortar, in order for it to be accommodated in the 2.5 mm thick joints, was based on an M7.5 mortar with adjusted granulometry after the removal of the coarsest aggregates. This mortar was subjected to flexural and compressive testing according

to the relevant standards for masonry mortar [11]. The small difference in the elastic stiffness of the units and the mortar ensures that the homogenisation scheme remains accurate in the prediction of the horizontal stiffness of the masonry composite in this case (Fig. 6a).

The two series of walls are illustrated in Fig. 8. For construction of the walls, the bricks were laid on their stretcher faces atop a template, the mortar being cast between the units. This accomplished uniformity in terms of mortar compaction and curing conditions, and therefore mechanical properties, between bed and head joints. The walls were capped with a concrete beam for evenly distributing the applied vertical load. In the case of the perforated walls, no lintel was provided above the window. The vertical prestress was applied through a hydraulic ram and kept constant. Horizontal load was applied in displacement control through a second hydraulic ram, oriented from left to right (Fig. 8). The walls were tested in a cantilever configuration, the top beam being allowed to rotate and displace freely in the vertical direction.

The experimental and numerically obtained values for the peak shear stress τ_{max} for the two series of walls are compared in tabulated form in Table 4 and graphically in terms of interaction diagrams in Fig. 9. The model is shown to be accurate in predicting the peak shear force for both series of walls, especially for lower magnitude vertical prestress levels. The model tends to slightly overestimate the peak shear force in the solid wall series, indicating a higher global effective shear modulus as understood at the level of the structural element [25]. Similarly, the model appears to slightly underestimate the peak shear force in the perforated wall series for a vertical prestress higher than 2.5 N/mm^2, at which point the model predictions are shifting to a failure mode dominated by compression [13].

The force–displacement graphs obtained in the experiments and in the numerical analyses are compared in Fig. 10. The initial global stiffness is calculated with high accuracy for all investigated cases. The overall curves are reproduced with very good accuracy in both series of experiments with the exception of the predicted force–displacement curve being steeper near the onset of yielding, particularly in the solid wall series with high vertical prestress. Nevertheless, the accuracy is comparable to the results obtained from a detailed micromodelling analysis of the same walls [15].

A comparison in the obtained failure modes is graphically provided in Fig. 11. Documentation of the damage in the experiments was performed manually at the end of the test, leading to potential perceptual subjectivity in the results and inability to capture the damage pattern at the precise moment of attaining peak force. The visible damage pattern in the numerical results is presented in terms of maximum principal strain, with the figure indicating strains corresponding to a crack width in excess of 0.1 mm, which is the minimum crack width clearly observable with the naked eye [30]. In the 2N20 case, the
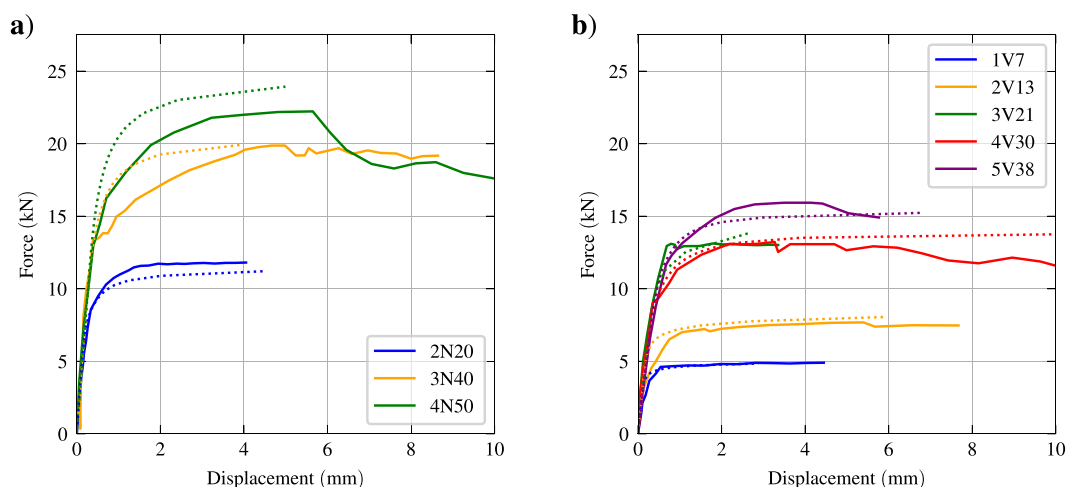

Fig. 10. Force-displacement graphs for walls under in plane shear. Comparison between experimental (dotted lines) and numerical (solid lines) results: a) solid, b) perforated walls.
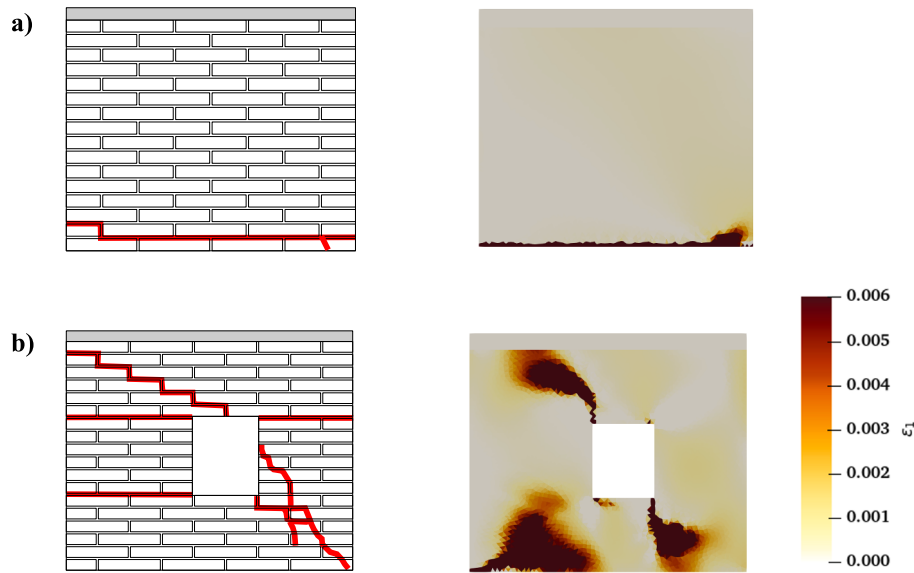
Fig. 11. Comparison of experimentally obtained (left) and numerically derived (right) crack patterns: a) 2N20 case and b) 3V21 case.
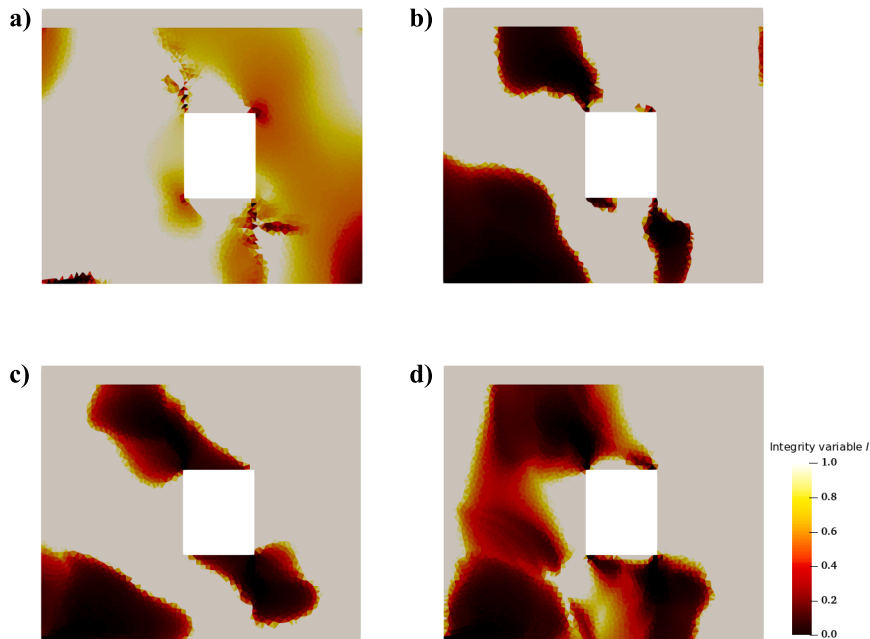

Fig. 12. Numerical integrity variables at peak force for the 3V21 case: a) compression of bed joints (I_c^b), b) tension of bed joints (I_t^b), c) tension of head joints (I_t^h) and d) shear of bed joints (I_v^b).

experimentally obtained failure mode primarily consists in a horizontal flexural crack forming at the base of the wall. This failure mode is accurately reproduced by the model. In the 3V21 case, the experimental crack pattern includes diagonal cracks initiating from the corners of the window opening and propagating to the edges of the wall. Additional horizontal cracks associated with post-peak rocking of the two piers are also formed near the base and top of the window opening. The model successfully reproduces the diagonal cracks, although the flexural cracks are formed at different locations, primarily near the base of the wall. The differences in the location of the flexural cracks could be attributed to differences in the boundary conditions at the top of the walls.

Finally, the damage as predicted by the model is presented in Fig. 12 in terms of integrity variables at peak force. This provides an additional layer of damage assessment and quantification that cannot be directly

derived from experimental data, especially regarding compressive damage. Plotting the integrity of the bed joints in compression (I_c^b) indicates the formation of a compressive strut in the right pier, with a plastic hinge being formed at the lower right corner of the wall (Fig. 12a). The right pier has a shorter length than the left pier, making it more susceptible to compressive damage under conditions of uniform vertical loading. The integrity of the bed joints in tension (I_t^b) indicates the formation of flexural failure near the left bases and right tops of both piers, also extending closer to the window, in agreement with experimental data (Fig. 12b). The integrity variable of the head joints in tension (I_t^h) indicates the location of diagonal cracks, extending from the window opening (Fig. 12c). Finally, the integrity variable of the bed joints in shear (I_v^b) indicates the onset of shearing damage at mid-height of the left pier, followed by shear slipping mostly concentrated at the

locations where opening of the head joints is also occurring (Fig. 12d).

6. Conclusions

The proposed computational homogenisation scheme, coupled with the proposed constitutive laws for compressive, tensile and shear damage, provides accurate linear and nonlinear results for a wide range of material combinations and case studies. Discrepancies between experimental or finite element analysis results and the predictions provided by the model are limited to extreme cases of material combinations characterised by mortar with extremely low stiffness compared to that of the units.

The model provides substantial advantages compared with finite element micromodelling, primarily in terms of computational cost and ease of results interpretation. Despite its lower modelling complexity, the model is able to provide comprehensive results on damage of the components of the masonry, including separately mapping damage to bed and head joints. Crack patterns can be clearly derived from the evaluation of the maximum principal strain, while assessment of the integrity variables in tension and compression at different components allows a more in-depth evaluation and quantification of the damage in the structure.

The low computational cost of the proposed method lends itself to its adoption as the computational component in digital twinning in combination with structural health monitoring operations for existing masonry buildings. In addition to generating macro-level analysis results, its capacity to provide stress, strain and damage data at the material component level makes the proposed model suitable to be combined with material-level structural health monitoring strategies such as those based on multi-functional materials (smart bricks and/or mortar).

Declaration of Competing Interest

The authors declare that they have no known competing financial interests or personal relationships that could have appeared to influence the work reported in this paper.

References

[1] Addessi D, Di Re P, Gatta C, Sacco E. Multiscale Analysis of Out-of-Plane Masonry Elements Using Different Structural Models at Macro and Microscale. Comput Struct 2021;247:106477. https://doi.org/10.1016/j.compstruc.2020.106477.

[2] Addessi D, Di Re P, Sacco E. Micromechanical and Multiscale Computational Modeling for Stability Analysis of Masonry Elements. Eng Struct 2020;211:110428. https://doi.org/10.1016/j.engstruct.2020.110428.

[3] Alnæs Martin S, Blechta Jan, Hake Johan, Johansson August, Kehlet Benjamin, Logg Anders, Richardson Chris, Ring Johannes, Rognes Marie E, Wells Garth N. The FEniCS Project Version 1.5. Arch Numer Softw 2015;3(100).

[4] Augusthus-Nelson Levingshan, Swift Gareth M. Experimental Investigation of the Residual Behaviour of Damaged Masonry Arch Structures. Structures 2020;27 (November 2019):2500–12.

[5] Benveniste Y. A New Approach to the Application of Mori-Tanaka's Theory in Composite Materials. Mech Mater 1987;6(2):147–57.

[6] Bati SB, Ranocchiai G, Ranocchiai G, Rovero L. A Micromechanical Model for Linear Homogenization of Brick Masonry. Mater Struct 1999;32(1):22–30.

[7] Bati SB, Ranocchiai G, Rovero L. Suitability of Micromechanical Model for Elastic Analysis of Masonry. J Eng Mech 1999;125(8):922–9.

[8] Cavalagli N, Cluni F, Gusella V. Evaluation of a Statistically Equivalent Periodic Unit Cell for a Quasi-Periodic Masonry. Int J Solids Struct 2013;50(25-26): 4226–40.

[9] Cavalagli N, Cluni F, Gusella V. Failure Surface of Quasi-Periodic Masonry by Means of Statistically Equivalent Periodic Unit Cell Approach. Meccanica 2018;53 (7):1719–36.

[10] Cecchi A, Sab K. A Homogenized Reissner-Mindlin Model for Orthotropic Periodic Plates: Application to Brickwork Panels. Int J Solids Struct 2007;44(18-19): 6055–79.

[11] CEN. EN 1015-11 — Methods of Test for Mortar for Masonry — Part 11: Determination of Flexural and Compressive Strength of Hardened Mortar; 2007.

[12] Drougkas A, Bejarano-Urrego L-E, Van Roy N, Verstrynge E. Macro Scale Material Characterisation in Support of Meso Scale Modelling of Masonry under Uniaxial In-Plane Loading. Int J Masonry Res Innov 2020;5(1):121–41.

[13] Drougkas A, Esposito R, Messali F, Sarhosis V. Analytical Models to Determine In-Plane Damage Initiation and Force Capacity of Masonry Walls with Openings. J Eng Mech 2021;147(11):04021088. https://doi.org/10.1061/(ASCE)EM.1943-7889.0001995.

[14] Drougkas A, Licciardello L, Rots JG, Esposito R. In-Plane Seismic Behaviour of Retrofitted Masonry Walls Subjected to Subsidence-Induced Damage. Eng Struct 2020;223:111192. https://doi.org/10.1016/j.engstruct.2020.111192.

[15] Drougkas A, Roca P, Molins C. Experimental Analysis and Detailed Micro-Modeling of Masonry Walls Subjected to In-Plane Shear. Eng Fail Anal 2019;95:82–95.

[16] Drougkas Anastasios, Sarhosis Vasilis. Micro-Mechanical Homogenisation of Three-Leaf Masonry Walls under Compression. Eng Struct 2021;245(November 2020).

[17] Drougkas A, Verstrynge E, Szekér P, Heirman G, Bejarano-Urrego L-E, Giardina G, et al. Numerical Modeling of a Church Nave Wall Subjected to Differential Settlements: Soil-Structure Interaction, Time-Dependence and Sensitivity Analysis. Int J Architect Heritage 2020;14(8):1221–38.

[18] Elmarakbi A, Jianhua W, Azoti WL. Non-Linear Elastic Moduli of Graphene Sheet-Reinforced Polymer Composites. Int J Solids Struct 2016;81:383–92.

[19] Eshelby JD. The Determination of the Elastic Field of an Ellipsoidal Inclusion, and Related Problems. Proc Royal Soc Lond Ser A Math Phys Sci 1957;241(1226): 376–96.

[20] Foulger GR, Wilson MP, Gluyas JG, Julian BR, Davies RJ. Global Review of Human-Induced Earthquakes. Earth Sci Rev 2018;178:438–514.

[21] García-Macías Enrique, Ubertini Filippo. Earthquake-Induced Damage Detection and Localization in Masonry Structures Using Smart Bricks and Kriging Strain Reconstruction: A Numerical Study. Earthquake Eng Struct Dyn 2018;July:1–22.

[22] Gumaste KS, Nanjunda Rao KS, Venkatarama Reddy BV, Jagadish KS. Strength and Elasticity of Brick Masonry Prisms and Wallettes under Compression. Mater Struct 2007;40(2):241–53.

[23] Lagomarsino S, Cattari S. PERPETUATE Guidelines for Seismic Performance-Based Assessment of Cultural Heritage Masonry Structures. Bull Earthq Eng 2015;13(1): 13–47.

[24] Lourenço PB, Pina-Henriques J. Validation of Analytical and Continuum Numerical Methods for Estimating the Compressive Strength of Masonry. Comput Struct 2006; 84(29-30):1977–89.

[25] Magenes G, Calvi GM. In-Plane Seismic Response of Brick Masonry Walls. Earthquake Eng Struct Dyn 1997;26(11):1091–112.

[26] Marzari N, Ferrari M. Textural and Micromorphological Effects on the Overall Elastic Response of Macroscopically Anisotropic Composites. J Appl Mech 1992;59 (2):269–75.

[27] Massart TJ, Peerlings RHJ, Geers MGD. Structural Damage Analysis of Masonry Walls Using Computational Homogenization. Int J Damage Mech 2007;16(2): 199–226.

[28] Massart TJ, Peerlings RHJ, Geers MGD. Mesoscopic Modeling of Failure and Damage-Induced Anisotropy in Brick Masonry. Eur J Mech A/Solids 2004;23(5): 719–35.

[29] Mori T, Tanaka K. Average Stress in Matrix and Average Elastic Energy of Materials with Misfitting Inclusions. Acta Metall 1973;21(5):571–4.

[30] Österberg G. Topography of the Layer of Rods and Cones in the Human Retina. Acta Ophthalmol 1935;13:6–97.

[31] Page AW. Finite Element Model for Masonry. J Struct Div ASCE 1978;104(8): 1267–85.

[32] Pelà L, Cervera M, Roca P. Continuum Damage Model for Orthotropic Materials: Application to Masonry. Comput Methods Appl Mech Eng 2011;200(9-12):917–30.

[33] Petracca M, Pelà L, Rossi R, Oller S, Camata G, Spacone E. Multiscale Computational First Order Homogenization of Thick Shells for the Analysis of Out-of-Plane Loaded Masonry Walls. Comput Methods Appl Mech Eng 2017;315: 273–301.

[34] Sarhosis V, Sheng Y. Identification of Material Parameters for Low Bond Strength Masonry. Eng Struct 2014;60:100–10.

[35] Taliercio A. Closed-Form Expressions for the Macroscopic in-Plane Elastic and Creep Coefficients of Brick Masonry. Int J Solids Struct 2014;51(17):2949–63.

[36] Theodossopoulos D, Sinha B. A Review of Analytical Methods in the Current Design Processes and Assessment of Performance of Masonry Structures. Constr Build Mater 2013;41:990–1001.

[37] Vermeltfoort AT, Martens DRW, van Zijl G. Brick–Mortar Interface Effects on Masonry under Compression. Can J Civ Eng 2007;34(11):1475–85.

[38] Voyiadjis GZ, Kattan PI. Mechanics of Damage, Healing, Damageability, and Integrity of Materials: A Conceptual Framework. Int J Damage Mech 2017;26(1): 50–103.

[39] Wilding BV, Godio M, Beyer K. The Ratio of Shear to Elastic Modulus of In-Plane Loaded Masonry. Mater Struct 2020;53(2):40.

[40] Zheng Q, Zhao Z, Du D. Irreducible Structure, Symmetry and Average of Eshelby's Tensor Fields in Isotropic Elasticity. J Mech Phys Solids 2006;54(2):368–83.

[41] Zou W, He Q, Huang M, Zheng Q. Eshelby's Problem of Non-Elliptical Inclusions. J Mech Phys Solids 2010;58(3):346–72.

[42] Zucchini A, Lourenço PB. A Micro-Mechanical Model for the Homogenisation of Masonry. Int J Solids Struct 2002;39(12):3233–55.

[43] Zucchini A, Lourenço PB. A Micro-Mechanical Homogenisation Model for Masonry: Application to Shear Walls. Int J Solids Struct 2009;46(3-4):871–86.